Nano Research
2023, 16(2): 2373–2382

ISSN 1998-0124 CN 11-5974/O4
https://doi.org/10.1007/s12274-022-4897-y

Research Article

$LiZr_2(PO_4)_3$ surface coating towards stable layer structure $Li_{1.2}Mn_{0.54}Ni_{0.13}Co_{0.13}O_2$ cathode materials with long cycle performance

Hao Yang, Jie Wang, Changsheng Xu, Kewei Wu, Fangfang Zou, Xuebu Hu (✉), and Zhongli Hu

College of Chemistry and Chemical Engineering, Chongqing University of Technology, Chongqing 400054, China

Received: 16 March 2022 / **Revised:** 10 August 2022 / **Accepted:** 11 August 2022

ABSTRACT

Li-rich manganese-based materials are considered to be the mainstream cathode materials for next-generation lithium-ion batteries due to high discharge capacity and low cost, but poor cycle life and high temperature performance limit their development. Herein, $LiZr_2(PO_4)_3$ (LZPO) is coated on the surface of spherical $Li_{1.2}Mn_{0.54}Ni_{0.13}Co_{0.13}O_2$ (LMNCO) material by a simple wet chemical method. The LZPO layer not only has the function of traditional coating layer to inhibit the occurrence of side reactions between electrolyte and LMNCO surface but also promotes the formation of spinel phase in the layered structure, increases the content of lattice oxygen, and reduces the content of absorbed oxygen. Thus, LZPO coated LMNCO has a more stable layered structure during cycling compared pure LMNCO, which improves effectively its long life and high temperature performance. The capacity loss rate of LZPO coated LMNCO is only 16.2% and 11.9% after 350 cycles at 25 °C and 200 cycles at 50 °C, respectively. Moreover, the capacity retention rate of the full cell composed of LZPO coated LMNCO and graphite is 70.7% after 200 cycles at 1.0 C. The coating layer toward stable surface structure can provide an idea for the modification of cathode materials, especially for Li-rich manganese-based materials.

KEYWORDS

$Li_{1.2}Mn_{0.54}N_{i0.13}Co_{0.13}O_2$, $LiZr_2(PO_4)_3$, layered structure, cycle life, high temperature

1 Introduction

In order to solve the problems of global energy shortage and environmental degradation, lithium-ion batteries have been widely used in power equipment [1]. Currently, the performance and price of lithium-ion battery cathode materials are the bottlenecks restricting their further development towards high energy, long life, and low cost [2]. Layered $Li_{1.2}Mn_{0.54}Ni_{0.13}Co_{0.13}O_2$ (LMNCO) as a cathode material has a high capacity (> 250 $mAh{\cdot}g^{-1}$) [3, 4], but there are still a series of problems to realize its commercialization. For example, initial low Coulombic efficiency is due to side reactions between active material and electrolyte under high voltage [5, 6]. Poor cycle is due to the destruction of the layered structure as the charge–discharge cycle process [7, 8], and poor rate performance is due to the low electronic conductivity of the Li_2MnO_3 phase [9, 10].

Nowadays, some studies found that the structural stability and cycle performance can be improved by changing part of layered structure into spinel phase or increasing the lattice oxygen content and reducing the adsorbed oxygen content. Song et al. synthesized TiO_2-coated LMNCO cathode material and found that the coated LMNCO had more lattice oxygen corresponding to a more stable layered structure [11]. Dong et al. synthesized Al_2O_3 and $LiAlO_2$-coated LMNCO cathode materials. The coating layer increased the lattice oxygen and reduced the absorbed oxygen so that the LMNCO had a more stable layered structure [12]. Wang et al. doped La^+ into LMNCO and a new redox peak appeared near 2.6 V. This was related to the insertion of lithium ions into the 16*c* position of the spinel, so the structural stability and cycle performance of the material were improved [13]. Chen et al. prepared LMNCO material with spinel phase by changing the synthesis method, and its rate performance and cycle stability were improved [14]. Nowadays, there is no article that clearly points out that the surface coating for LMNCO can not only increase the lattice oxygen content and reduce the absorbed oxygen content but also promote the formation of spinel phase in the layered structure of Li^+. sodium super ion conductor (NASICON)-type $LiZr_2(PO_4)_3$ (LZPO) exhibits ultra-high lithium-ion conductivity. Due to its unique phosphate structure, interstitial space in large open frame, high stability, and small volume change during cycling, LZPO can be used as an excellent solid electrolyte [15]. Here we used LZPO as a surface layer act the traditional coating function for the LMNCO material. LZPO can not only induce the formation of $LiMn_2O_4$ spinel phase but also increase the lattice oxygen content and reduce the absorbed oxygen content. Furthermore, the coated LMNCO had lower Li^+/Ni^{2+} mixing. Therefore, LZPO-coated LMNCO had excellent electrochemical performances.

In this work, LZPO was coated on the spherical LMNCO surface by simple wet chemistry. The thin LZPO layer improved the stability of LMNCO layered structure, which enhanced its long-cycle performance at room and high temperature. The average capacity loss per cycle for 350 and 200 cycles at 25 and 50 °C was

Address correspondence to xuebu@cqut.edu.cn

only 0.0463% and 0.0595%, respectively. LZPO surface coating was a good strategy to improve the electrochemical performances of lithium-rich manganese-based cathode materials.

2 Experimental

2.1 Synthesis of LMNCO material

The $Mn_{4/6}Ni_{1/6}Co_{1/3}CO_3$ precursor was synthesized through the traditional co-precipitation method and then mixed with lithium source under high temperature calcination to prepare LMNCO [16].

To prepare LZPO coated LMNCO, $NH_4H_2PO_4$, $LiNO_3$, and $Zr(NO_3)_4$ were dissolved in the ethanol (C_2H_5OH) solution according to theoretical molar ratio, slowly stirred to obtain the precursor, then added a certain mass of LMNCO powder to the solution, and stirred the mixture at 80 °C until ethanol was evaporated completely. The mixture was calcined at 750 °C for 1 h in an oxygen atmosphere at a heating rate of 5 °C·min^{-1}. The LZPO coated LMNCO was marked as LZPO-LMNCO. The content of LZPO in the composite was 3 wt.%.

2.2 Physical characterization

The phase composition and lattice structure of all samples were analyzed by X-ray diffraction (XRD, Cu Kα: λ = 0.154056 nm, V = 40 kV, I = 30 mA, 2θ = 10°–80°). The Rietveld refinement of the relevant XRD data was calculated using GSAS software. Raman spectra were carried out on Horiba Jobin Yvon LabRAM HR800 Raman spectrometer with a 532 nm light source. Micro-morphological characters were observed by scanning electron microscope (SEM, QUANTA FEG 400) and transmission electron microscope (TEM, FEI Tecnai G2 F20). The element distribution spectrometer (EDS) and X-ray photoelectron spectroscopy (XPS, Thermo Fisher-VG Scientific ESCALAB 250Xi) were implemented to observe the surface element distribution and valence state.

2.3 Electrochemical characterization

N-Methyl-2-pyrrolidone was used as a solvent, active material, polyvinylidene fluoride, and acetylene black were uniformly mixed at a mass ratio of 8:1:1 to prepare a cathode slurry. As-prepared slurry was evenly coated on aluminum foil, then vacuum dried at 120 °C for 12 h. The dried aluminum foil was cut into a wafer with an area of 1.54 cm^2 as the cathode. Lithium sheet was used as anode. The electrolyte was 1.0 M $LiPF_6$ (the volume ratio of ethylene carbonate:ethyl methyl carbonate:dimethyl carbonate = 1:1:1). The electrochemical properties of the material were assembled into a half-cell by CR-2032 and tested on LAND battery test system (LAND CT2001A; Wuhan, China) with a voltage window of 2.0–4.8 V (vs. Li/Li$^+$). Cyclic voltammetry (CV) was studied by DH7000 (Jiangsu Donghua Analytical Instruments Co., Ltd) with a voltage range of 2.0–4.8 V and a scan rate of 0.1 mV·s^{-1}. The same electrochemical workstation was used to collect electrochemical impedance spectroscopy (EIS).

3 Results and discussion

The XRD diffraction patterns of the samples are shown in Fig. 1(a). Obviously, the XRD diffraction peaks of two samples were indexed to the hexagonal α-$NaFeO_2$ structure with $R\bar{3}m$ group space [17–19]. There was a weak diffraction peak between 20° and 30°, which was caused by the formation of the Li_2MnO_3 phase of the $C2/m$ space group [20, 21]. The clear split peaks of (006)/(102) and (108)/(110) indicated that both samples had a highly ordered layered structure [22, 23]. The above results implied that LZPO coating LMNCO did not change the layered structure of LMNCO. Significantly, the XRD diffraction patterns in LZPO-LMNCO showed no characteristic peak of LZPO, which was due to low content of LZPO in the composite. Figure S1 in the Electronic Supplementary Material (ESM) showed XRD result of 10 wt.% LZPO-LMNCO. Clearly, the characteristic peaks of LZPO appeared in the patterns, indicating the existence of LZPO in the composite. In order to obtain more detailed crystal structure data, the XRD data of two samples were refined by Rietveld, and the refined results are shown in Figs. 1(b) and 1(c), and Table 1. The small values of R_{wp}, R_p, and χ^2 (R_{wp}: weighted profile factor, R_p: profile factor, and χ^2: goodness of fit indicator) for the samples indicated a good fit with the Rietveld refinements [24]. The c/a

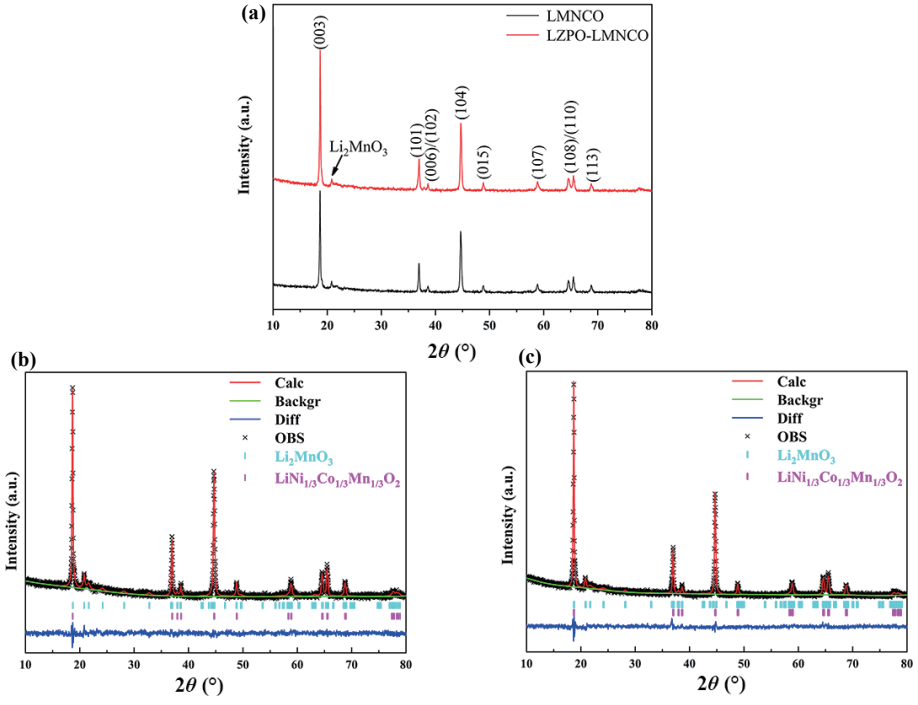

Figure 1 (a) XRD diffraction patterns of LMNCO and LZPO-LMNCO; and XRD Rietveld refinement results of (b) LMNCO and (c) LZPO-LMNCO.

Table 1 Rietveld refinement results of XRD statistic for the samples

Sample	a (Å)	c (Å)	c/a	$I_{(003)}/I_{(104)}$	V (Å)^3	R_{wp} (%)	R_p (%)	χ^2 (%)
LMNCO	2.8483	14.2271	4.9949	1.4599	99.9606	2.23	1.77	1.45
LZPO-LMNCO	2.8483	14.2183	4.9918	1.7530	99.9030	2.26	1.76	1.61

values of LMNCO and LZPO-LMNCO were 4.9949 and 4.9918, respectively, which are both higher than 4.9, indicating a good layered structure for two samples [25]. It was generally believed that the ratio of $I_{(003)}/I_{(104)}$ indicates the level of Li^+/Ni^{2+} mixing [26, 27]. Thus, an increase in the ratio of $I_{(003)}/I_{(104)}$ indicated a decrease in Li^+/Ni^{2+} mixing. The values of $I_{(003)}/I_{(104)}$ in LMNCO and LZPO-LMNCO were 1.4599 and 1.7530, respectively, indicating that the latter had lower Li^+/Ni^{2+} mixing degree and better cycle performance.

In order to prove that LZPO was wrapped on the surface of LMNCO, the electron microscopy was used to study it. As shown in Figs. 2(a), 2(b), 2(d), and 2(e), both LMNCO and LZPO-LMNCO were secondary spherical particles with a diameter of approximately 18.5 μm. The surface of LZPO-LMNCO was relatively rougher, which was due to the LZPO layer on the surface. In Figs. 2(c) and 2(f), it could be seen from the enlarged high-resolution TEM (HRTEM) images that the same lattice spacing (0.472 nm) of LMNCO and LZPO-LMNCO were obvious and continuous, which corresponded to the (003) crystal plane of LMNCO. Furthermore, there was a thin coating layer on the surface, and the lattice spacing of 0.318 nm corresponded to the (400) crystal plane of LZPO coating layer in Fig. 2(f). The above results indicated there was the presence of LZPO in the LZPO-LMNCO composite and the crystal structure of LMNCO had not changed after LZPO surface modification. In order to further prove that the coating was LZPO, EDS was applied for elemental analysis, and the results are shown in Fig. 2(h). Obviously, Zr and P elements are evenly distributed on the surface of LMNCO, indicating that LZPO was coated on the surface of LMNCO.

XPS measurement was applied to analyze the chemical state and element valence to more accurately prove the existence of LZPO on the surface. As shown in Fig. 3(a), four elements, Ni, Co,

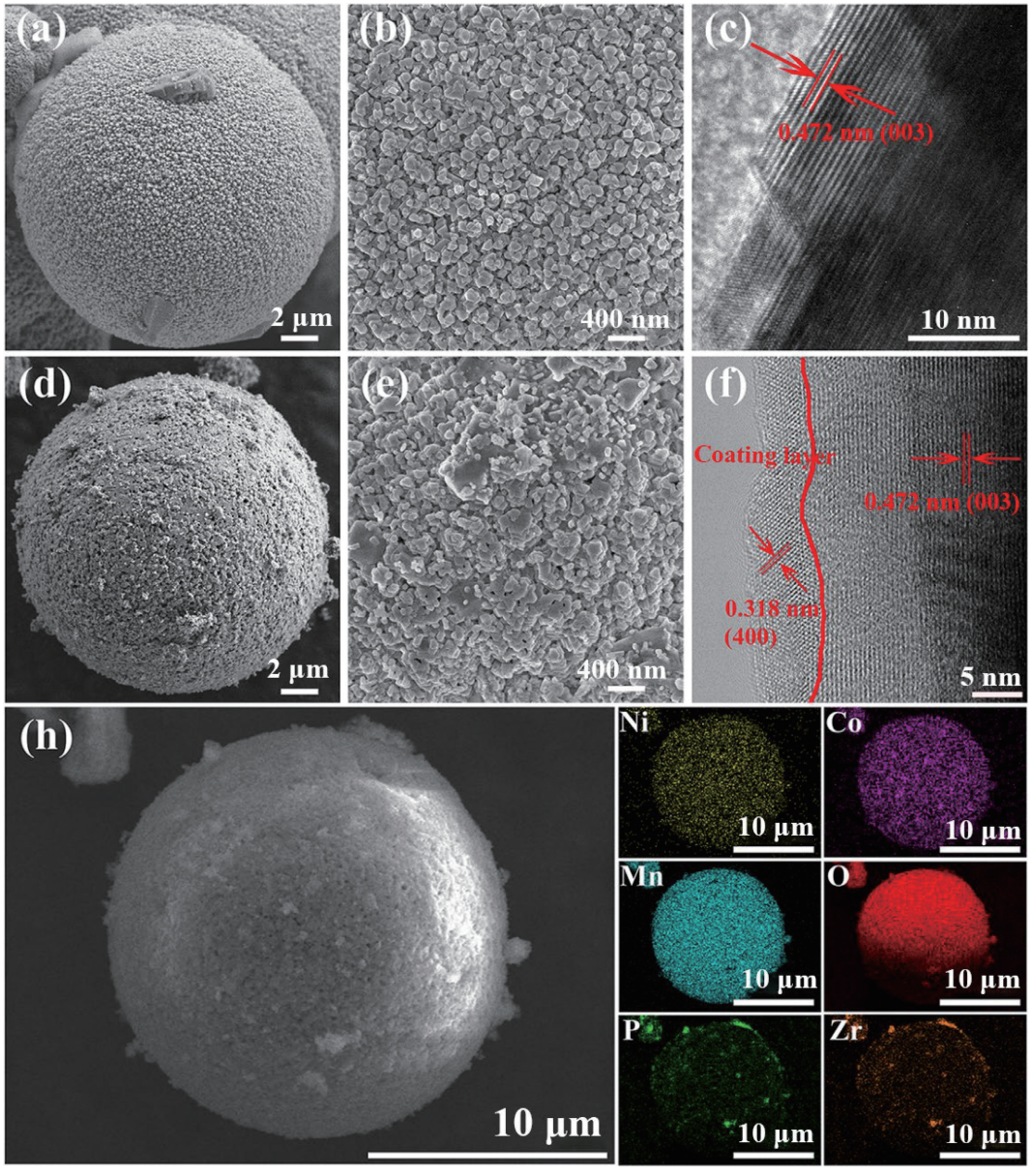

Figure 2 SEM and HRTEM images of (a)–(c) LMNCO and (d)–(f) LZPO-LMNCO; and (h) EDS mapping images of LZPO-LMNCO.

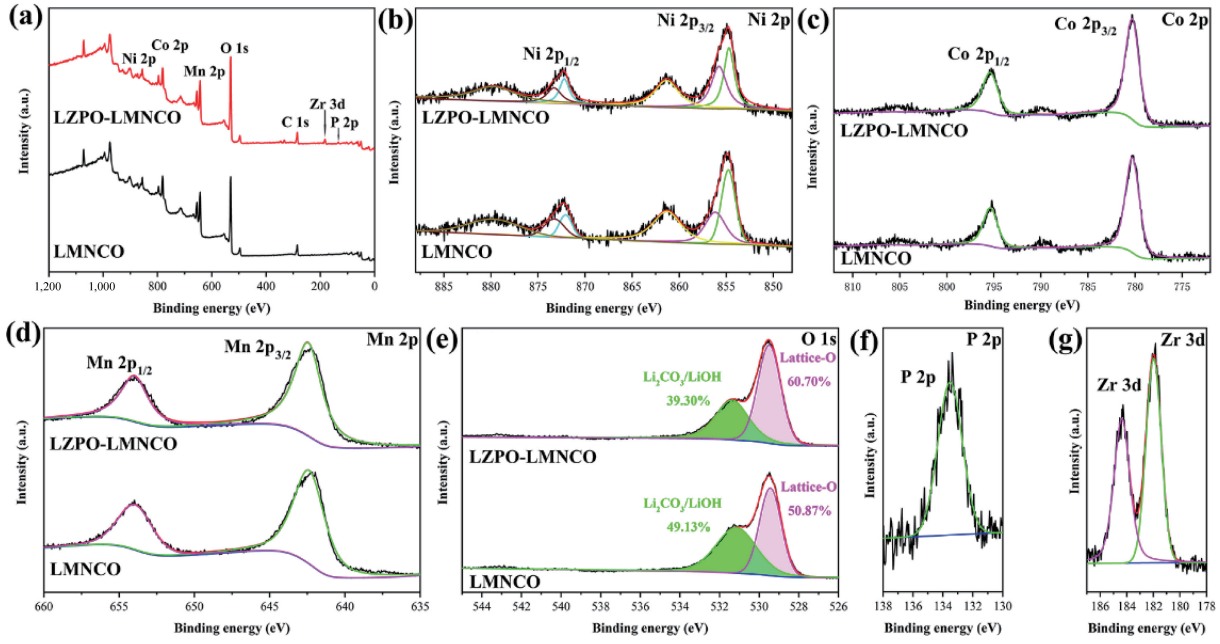

Figure 3 XPS images of (a) full pattern, (b) Ni 2p, (c) Co 2p, (d) Al 2p, and (e) O 1s for LMNCO and LZPO-LMNCO; and (f) P 2p and (g) Zr 3d for LZPO-LMNCO.

Mn, and O, were detected for LMNCO and the additional P and Zr elements for LZPO-LMNCO. It could be found that the characteristic peaks of Ni 2p, Co 2p, and Mn 2p were not significantly different in two samples [28]. Due to the presence of Li_2CO_3 and LiOH on the surface of the powder, the peak at 531.5 eV in the O 1s spectrum corresponds to the presence of absorbed oxygen ($O_{absorbed}$), and a peak at 529.3 eV was attributed to the presence of lattice oxygen ($O_{lattice}$) [29, 30]. Obviously, the LZPO-LMNCO had more lattice oxygen (60.70%) and less absorbed oxygen (39.30%). By comparison, LMNCO had less lattice oxygen (50.87%) and more absorbed oxygen (49.13%). The increase in the amount of lattice oxygen indicated that the LZPO coating layer enhanced the metal bond energy so that LZPO had a more stable layered structure and better electrochemical performances [31]. Besides, Li_2CO_3 and LiOH on the surface of the particles can be used as part of the lithium source to react to form LZPO, so LZPO-LMNCO had less inactive Li_2CO_3 and LiOH compared to pure LMNCO[24, 32].TheP2ppeakat133.4eVandtheZr3dpeaksat181.9and 184.4 eV were clearly detected. The results demonstrated that the valence states of Zr 3d and P 2p were consistent with LZPO as Zr^{4+} and P^{3+}, respectively. Therefore, LZPO-coated LMNCO can increase the content of lattice oxygen and reduce the content of absorbed oxygen, so LZPO-LMNCO had a more stable layered structure.

Figure 4(a) showed initial charge/discharge curves of LMNCO and LZPO-LMNCO at 0.1 C (1 C = 250.0 mAh·g^{-1}). All curves had two voltage plateaus near 4.0 and 4.5 V, which was the main characteristics of lithium-rich materials. The two voltage plateaus corresponded to two oxidation peaks of initial CV in Fig. 4(b). The oxidation of Ni^{2+} and Co^{3+} were related to first oxidation peak near 4.0 V, which was mainly due to the extraction of Li^+ from $LiNi_{1/3}Co_{1/3}Mn_{1/3}O_2$ [33–35]. The second oxidation peak near 4.5 V was related to the release of Li^+ from the Li_2MnO_3 phase and accompanied by irreversible oxygen release and structural reorganization [36, 37], which was the main reason for large irreversible loss of its capacity. Obviously, LZPO-LMNCO had a longer voltage plateau than LMNCO, indicating that LZPO coating could enhance the activity of the Li_2MnO_3 phase. Therefore, it had a higher discharge specific capacity (276.3 mAh·g^{-1}) compared to LMNCO (260.0 mAh·g^{-1}). There was a reduction peak at 2.55 V in the CV of twos samples, which was consistent with the results of the discharge platform. This was concerned with Li^+ insert into the 16*c* octahedral sites in spinel [13, 14, 38]. The enlarged view in the CV was embedded in Fig. 4(b). As shown in the figure, this phenomenon in LZPO-LMNCO is more obvious than in LMNCO, indicating that LZPO surface modification induced the formation of spinel in the material. Clearly, as shown in Fig. 4(c), there was $LiMn_2O_4$ spinel phase in the bulk phase, and the lattice spacing was 0.248 nm, corresponding to the (311) crystal plane of $LiMn_2O_4$ spinel phase. The peak of $LiMn_2O_4$ spinel phase appeared in the Raman spectrum of Fig. 4(d), which further indicated that $LiMn_2O_4$ spinel phase existed in LZPO-LMNCO [39]. The introduction of spinel phase into the layered structure could improve the structural stability of LMNCO so that LZPO-LMNCO had higher discharge capacity.

In order to deeply explore the influence of LZPO on the electrochemical performances of LMNCO, the cycle test was carried out at 1.0 C and 25 °C, and the results are shown in Fig. 5. The capacity and capacity retention ratio of LMNCO were only 156.0 mAh·g^{-1} and 75.1% after 100 cycles, respectively. The values of LZPO-LMNCO still possessed 180.4 mAh·g^{-1} and 83.8% even after 350 cycles. The results proved that LZPO surface modification could improve remarkably long cycle performance of LMNCO. On the one hand, the LZPO layer prevented the direct contact between LMNCO and the electrolyte and alleviated the corrosion of the electrolyte to the active material, thereby improving the stability of its layered structure. On the other hand, the LZPO was an ultrafast lithium-ion conductor, which may increase the diffusion rate of Li^+ at the interface. In Fig. 5(c), the LZPO-LMNCO still showed a weak voltage plateau near 2.5 V after first 100 cycles, which further illustrated that LZPO promotes the insertion of Li^+ into the 16*c* octahedral site in the spinel. The spinel phase can stabilize the layered structure, so the LZPO-LMNCO behaved better cycle performance.

Figures 5(d) and 5(e) showed the d*Q*/d*V* curves of the materials at 25 °C and 1.0 C with different cycles. The reduction peak near 3.25 V was related to $Mn^{4+/3+}$. As the cycle progressed, the reduction peak for LMNCO and LZPO-LMNCO gradually shifted to a lower potential. This showed that the material had gradually changed from a layered structure to a spinel structure. Finally, a new reduction peak was formed at about 2.7 V, which represented

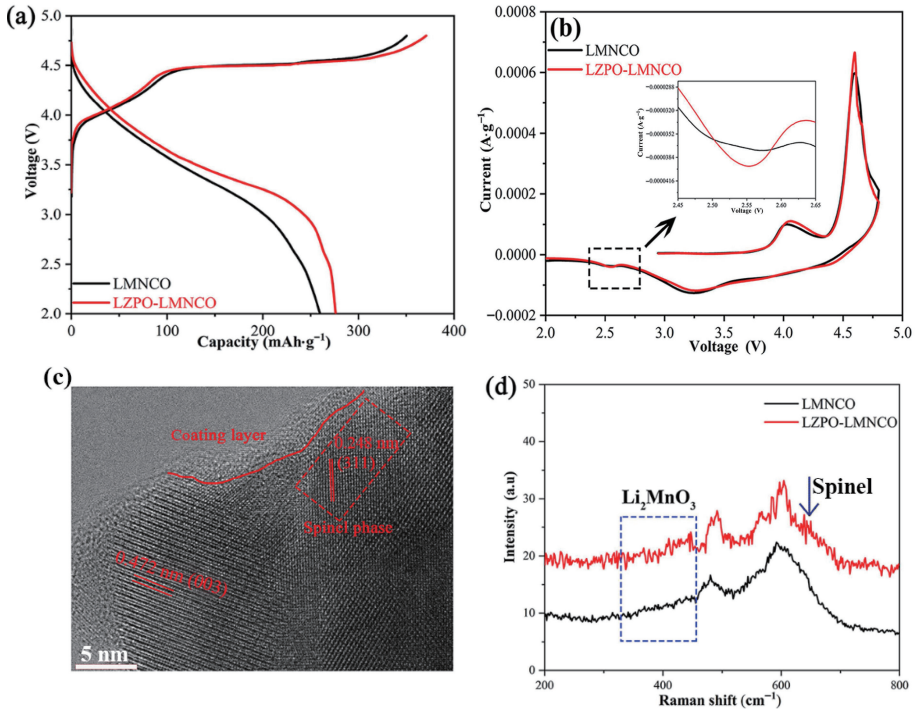

Figure 4 (a) Initial charge/discharge curves and (b) CV of LMNCO and LZPO-LMNCO at 25 °C; (c) HRTEM of LZPO-LMNCO; and (d) Raman spectra of LMNCO and LZPO-LMNCO.

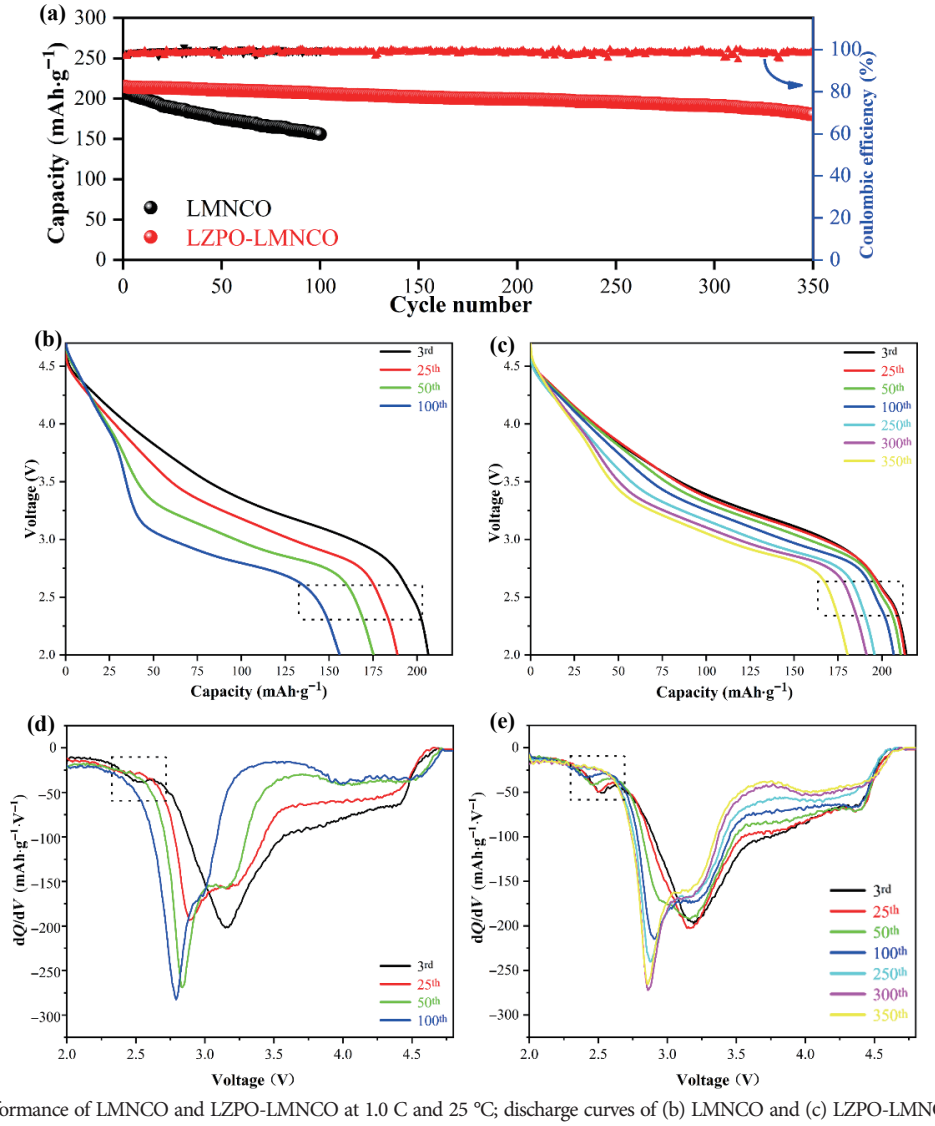

Figure 5 (a) Cycle performance of LMNCO and LZPO-LMNCO at 1.0 C and 25 °C; discharge curves of (b) LMNCO and (c) LZPO-LMNCO; and corresponding dQ/dV curves of (d) LMNCO and (e) LZPO-LMNCO.

a phase transition of the material from layer to spinel. However, the LZPO-LMNCO still retained a reduction peak near 3.25 V, which proved that it had more layered structure. In addition, the LZPO-LMNCO has a weak reduction peak near 2.55 V. This was related to the reinsertion of Li^+ into the spinel $LiMn_2O_4$ structure. Therefore, the modified LMNCO of LZPO had a more stable layered structure.

Figure 6 showed the cycle performance of the electrodes at 50 °C and 1.0 C. Obviously, the LZPO-LMNCO electrode showed a higher discharge capacity than the LMNCO. The discharge capacity was 185.0 mAh·g^{-1} after 200 cycles, and the corresponding capacity retention ratio was 88.1%. The LMNCO electrode only delivered a capacity of 157.2 mAh·g^{-1} after 80 cycles with the capacity retention of 75.3%. The results illustrated that high temperature performance of LMNCO after LZPO surface modification had also been improved. It may be because the LZPO coating reduced the direct contact between LMNCO and the electrolyte, which relieved the dissolution of transition metal ions, and thus has more stable high temperature performance for LMNCO. As shown in Figs. 6(b) and 6(c), the discharge curve of two electrodes at 50 °C is similar to that at 25 °C, indicating that the intercalated spinel phase in the layered structure also occurs at high temperature.

The rate performance test of the electrodes was implemented at 25 °C, and the results are shown in Fig. 7(a). Clearly, the LZPO-LMNCO electrode delivered high average discharge capacities of 273.5, 250.1, 229.6, 211.6, 173.1, 151.0, and 267.1 mAh·g^{-1} at 0.1, 0.2, 0.5, 1.0, 2.0, 5.0, and 0.1 C, respectively. However, the corresponding values in the LMNCO were 255.9, 233.1, 217.4, 205.2, 158.5, 123.6, and 248.4 mAh·g^{-1}. The LZPO-LMNCO exhibited better rate performance. The possible reason was that the existence of the LZPO layer increased the diffusion rate of lithium ions. In addition, the LZPO-LMNCO had lower cation mixing resulting in higher electrochemical activity [40].

To understand the reaction mechanism and high rate performance of the LZPO-LMNCO, EIS of the electrodes was performed. Figure 7 showed EIS results of the electrodes before and after cycles in order to verify that LZPO improved lithium-ion diffusion rate. The equivalent circuit diagram was inserted into the figures. The curves of the electrodes consisted of a semicircle in the middle and high frequency region and a straight line in the low frequency region. The semicircle corresponds to charge transfer impedance (R_{ct}) of the electrolyte and electrode interface, and the straight line corresponds to Warburg impedance of lithium-ion diffusion (ω_o). Furthermore, the fitted data via Z-view software are shown in Table 2. According to the results, the interface resistance of $R_s + R_{ct}$ in LMNCO increased rapidly from 86.97 Ω before cycle to 480.69 Ω after 100 cycles. However, the corresponding value in the LZPO-LMNCO changed from 54.93 to 229.93 Ω. Obviously, LZPO surface modification LMNCO significantly reduced the increase of the impedance, implying better charge transfer ability during cycling. In addition, Eq. (1) was used to estimate lithium-ion diffusion coefficients (D_{Li^+}) [41, 42]

$$D_{Li^+} = \frac{R^2T^2}{2A^2n^4F^4C^2\sigma^2} \quad (1)$$

$$Z' = R_s + R_{ct} + \sigma\omega^{-1/2} \quad (2)$$

where A, F, R, T, C, and n represented electrode surface area (1.54 cm^2), Faraday constant (96,500 C·mol^{-1}), gas constant (8.314 J·K^{-1}), absolute temperature (298 K), the concentration of lithium-ions, and the number of electrons, respectively. There was a linear relationship between Warburg coefficient (σ) and real impedance (Z') in Eq. (2) [43, 44]. The lithium-ion diffusion coefficients of LZPO-LMNCO before and after cycling were larger than those of LMNCO. LZPO surface modification LMNCO had high lithium-ion diffusivity and excellent reaction kinetics.

The XRD results of the samples after long cycle are shown in Fig. 8(a). The larger the value of $I_{(003)}/I_{(104)}$, the lower Li^+/Ni^{2+} mixing degree [26, 27]. The $I_{(003)}/I_{(104)}$ ratios of LZPO-LMNCO and LMNCO samples were 2.2113 and 1.7442, respectively, which shown that the LZPO-LMNCO was more stable than the LMNCO after long cycle. Figures 8(b) and 8(c) showed SEM of LMNCO and LZPO-LMNCO after 100 cycles at 1.0 C and 25 °C. There was a clear difference between LZPO and LZPO-LMNCO. Obviously, the surface of LMNCO was severely damaged, while

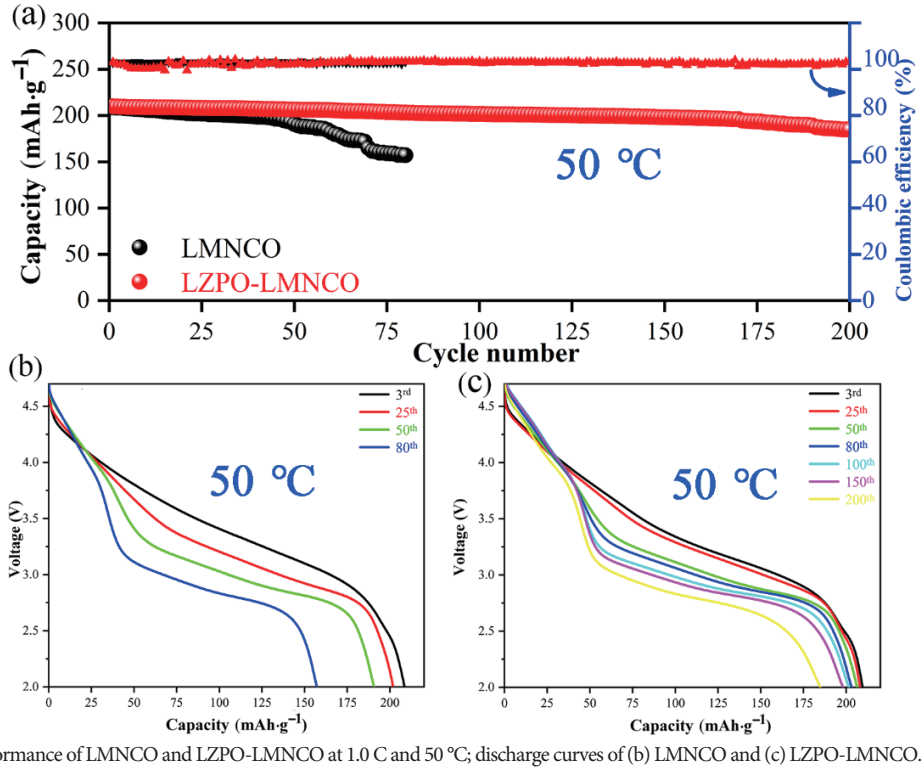

Figure 6 (a) Cycle performance of LMNCO and LZPO-LMNCO at 1.0 C and 50 °C; discharge curves of (b) LMNCO and (c) LZPO-LMNCO.

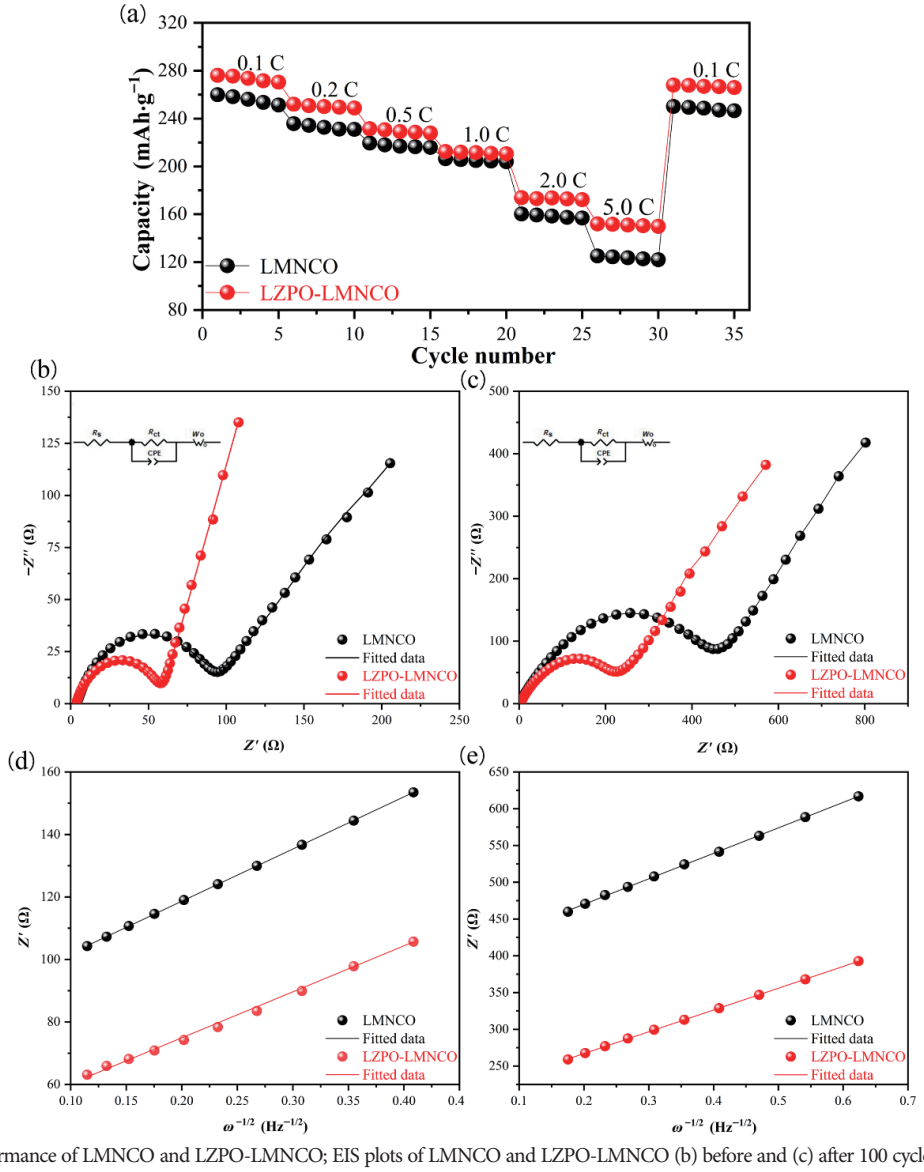

Figure 7 (a) Rate performance of LMNCO and LZPO-LMNCO; EIS plots of LMNCO and LZPO-LMNCO (b) before and (c) after 100 cycles; the linear relationship of Z' and $\omega^{-1/2}$ of LMNCO and LZPO-LMNCO (d) before and (e) after 100 cycles.

Table 2 The results of the fitted data and lithium-ion diffusion coefficients

Sample	Before the cycle			After 100 cycles		
	$R_s + R_{ct}$ (Ω)	σ	D_{Li^+} (cm^2·s^{-1})	$R_s + R_{ct}$ (Ω)	σ	D_{Li^+} (cm^2·s^{-1})
LMNCO	86.97	169.24	7.83×10^{-16}	480.69	347.92	1.85×10^{-16}
LZPO-LMNCO	54.93	147.19	1.04×10^{-15}	229.93	296.29	2.81×10^{-16}

the surface of LZPO-LMNCO was relatively intact. Side reactions of the electrolyte with the LMNCO led to the reorganization of the surface structure and the increase of the impedance. On the contrary, the presence of the LZPO coating layer inhibited the side reaction between the electrolyte and the LMNCO. Therefore, LZPO-LMNCO has better structural stability compared with LMNCO, which can improve the cycle performance of the materials.

The electrochemical performances of the full cells were studied with graphite as anode, LMNCO, and LZPO-LMNCO as cathode, respectively. Figures 9(a) and 9(b) showed the charge/discharge curves of the electrodes at 0.1 C. As shown in the figures, the charge/discharge capacities of LMNCO, LZPO-LMNCO, and graphite were 350.5/260.0, 370.8/276.3, and 315.8/402.3 mAh·g^{-1}, respectively, and the corresponding coulombic efficiencies were 74.2%, 74.5%, and 78.5%. As shown in Fig. 9(c), the charge/discharge capacities of LMNCO/graphite and LZPO-LMNCO/graphite were 335.2/232.3 and 345/246.3 mAh·g^{-1}, respectively, and the corresponding coulomb efficiencies were 69.3% and 71.4%. Compared with LMNCO/graphite, the slight increase of LZPO-LMNCO/graphite discharge capacity was attributed to the fact that LZPO coating can improve the activity of Li_2MnO_3 phase and induce the appearance of $LiMn_2O_4$ spinel phase. Its initial Coulombic efficiency was increased because LZPO coating can inhibit the side reaction between active material and electrolyte. Figure 9(d) showed cycle performance of the full batteries at 1.0 C. After 200 cycles, the remaining capacities of LMNCO/graphite and LZPO-LMNCO/graphite reached 71.23 and 115.5 mAh·g^{-1}. The corresponding capacity retention rates were 51.6% and 70.7%, respectively. Meanwhile, the Coulombic efficiency of LZPO-LMNCO/graphite was slightly higher than that of LMNCO/graphite during cycling because the appearance of spinel phase can make the structure more stable and the coating can inhibit the side reactions between the active material and the

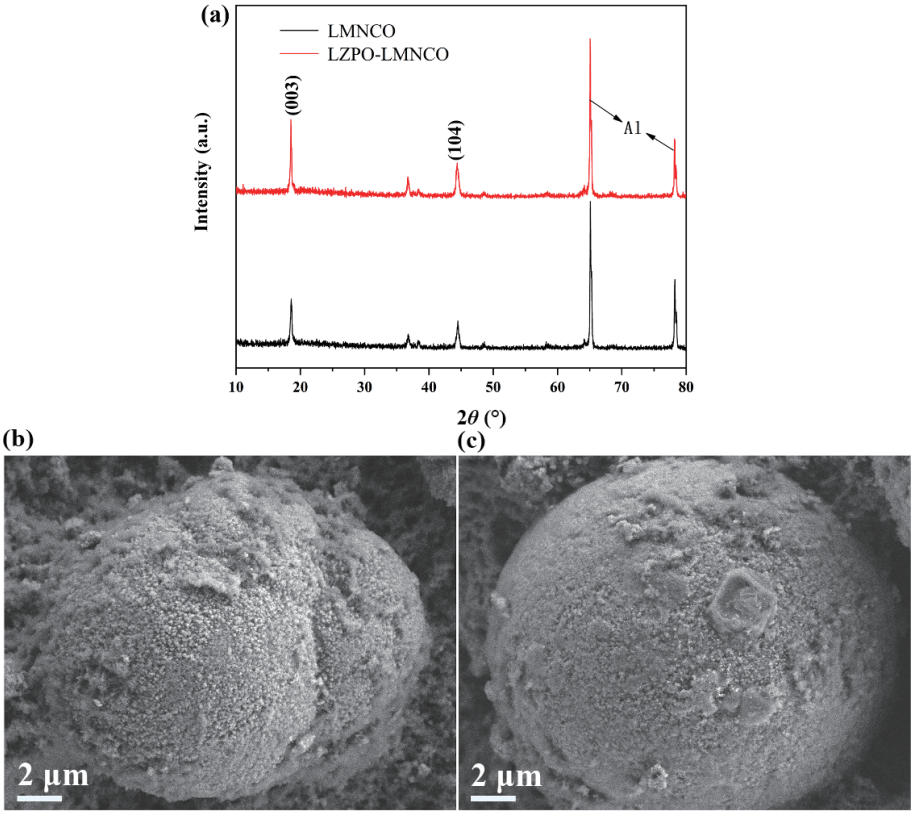

Figure 8 (a) XRD diffraction patterns of LMNCO and LZPO-LMNCO after 200 cycles; SEM of (b) LMNCO and (c) LZPO-LMNCO after 100 cycles at 1.0 C and 25 °C.

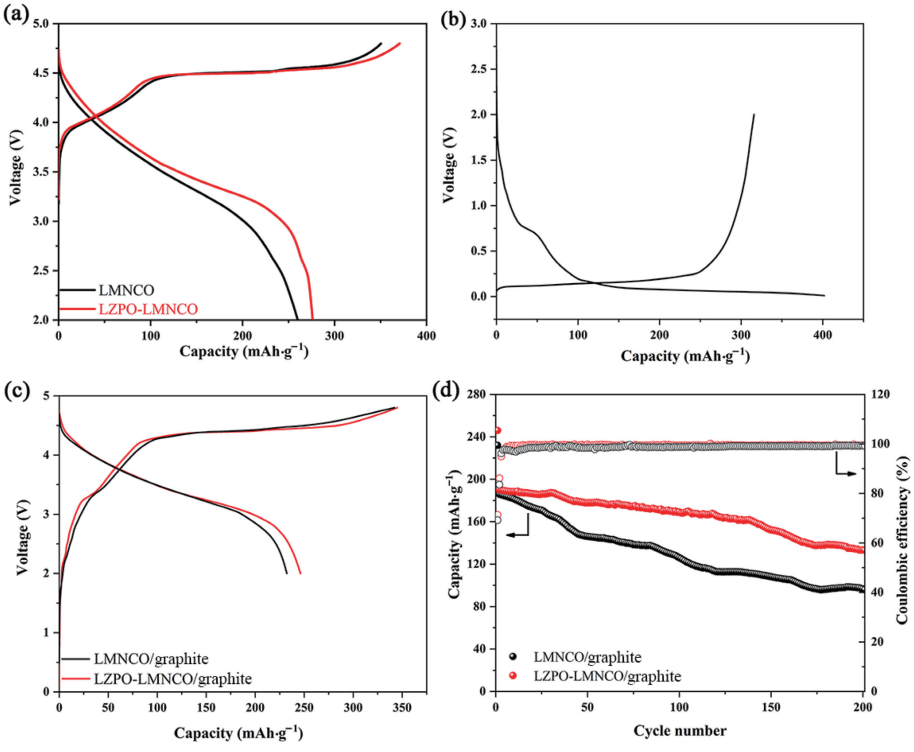

Figure 9 Initial charge/discharge curves in lithium half-cells of (a) LMNCO and LZPO-LMNCO and (b) graphite at 0.1 C; (c) initial charge/discharge curves at 0.1 C and (d) cycle performance at 1 C of full cells.

electrolyte. These results showed that LZPO-LMNCO had good cycle performance, which made it possible to develop in the practical application of lithium-ion batteries.

4 Conclusions

In summary, spherical LZPO-coated LMNCO has been successfully synthesized. Physical characterizations prove that LZPO-LMNCO has lower Li^+/Ni^{2+} mixing, more lattice oxygen content, and less absorbed oxygen content so that it has a more stable layered structure compared with LMNCO. Electrochemical characterizations show that LZPO promotes Li^+ into $LiMn_2O_4$ spinel structure during cycling, and the introduction of spinel phase into the layered structure improves the structural stability of

LMNCO. Therefore, LZPO-LMNCO composite exhibit excellent long-cycle performance at both room and high temperature. The discharge capacity and capacity retention rate of LMNCO are only 156.0 mAh·g^{-1} and 75.1% after 100 cycles at 1.0 C and 25 °C. The values of LZPO-LMNCO still possessed 180.4 mAh·g^{-1} and 83.8% even after 350 cycles. Even at 50 °C, the LMNCO only delivers a capacity of 157.2 mAh·g^{-1} after 80 cycles with the capacity retention of 75.3%, but the LZPO-LMNCO delivers a capacity of 185.0 mAh·g^{-1} after 200 cycles with the capacity retention of 88.1%. And the remaining capacities of LMNCO/graphite and LZPO-LMNCO/graphite reach 71.23 and 115.5 mAh·g^{-1} after 200 cycles at 1.0 C. The corresponding capacity retention rates were 51.6% and 70.7%, respectively. Therefore, this functional coating material can provide a reference for further research on Li-rich manganese-based materials.

Acknowledgements

This work received support from the Key Project of Science and Technology Research of Chongqing Education Commission of China (No. KJZDK201801103), the Venture & Innovation Support Program for Chongqing Overseas Returnees (No. cx2019128), and Scientific Research Foundation of Chongqing University of Technology (No. 2022ZDZ004).

Electronic Supplementary Material: Supplementary material (XRD diffraction pattern of 10 wt.% LZPO-LMNCO) is available in the online version of this article at https://doi.org/10.1007/s12274-022-4897-y.

References

[1] Kim, T.; Song, W. T.; Son, D. Y.; Ono, L. K.; Qi, Y. B. Lithium-ion batteries: Outlook on present, future, and hybridized technologies. *J. Mater. Chem. A* **2019**, *7*, 2942–2964.

[2] Hy, S.; Liu, H. D.; Zhang, M. H.; Qian, D. N.; Hwang, B. J.; Meng, Y. S. Performance and design considerations for lithium excess layered oxide positive electrode materials for lithium ion batteries. *Energy Environ Sci.* **2016**, *9*, 1931–1954.

[3] Lei, Y. K.; Ni, J.; Hu, Z. J.; Wang, Z. M.; Gui, F. K.; Li, B.; Ming, P. W.; Zhang, C. M.; Elias, Y.; Aurbach, D. et al. Surface modification of Li-rich Mn-based layered oxide cathodes: Challenges, materials, methods, and characterization. *Adv. Energy Mater.* **2020**, *10*, 2002506.

[4] Li, Y. W.; Li, Z. B.; Chen, C.; Yang, K.; Cao, B.; Xu, S. Y.; Yang, N.; Zhao, W. G.; Chen, H. B.; Zhang, M. J. et al. Recent progress in Li and Mn rich layered oxide cathodes for Li-ion batteries. *J. Energy Chem.* **2021**, *61*, 368–385.

[5] Nayak, P. K.; Erickson, E. M.; Schipper, F.; Penki, T. R.; Munichandraiah, N.; Adelhelm, P.; Sclar, H.; Amalraj, F.; Markovsky, B.; Aurbach, D. Review on challenges and recent advances in the electrochemical performance of high capacity Li- and Mn-rich cathode materials for Li-ion batteries. *Adv. Energy Mater.* **2018**, *8*, 1702397.

[6] Liu, Y. Y.; Yang, Z.; Zhong, J. J.; Li, J. L.; Li, R. R.; Yu, Y.; Kang, F. Y. Surface-functionalized coating for lithium-rich cathode material to achieve ultra-high rate and excellent cycle performance. *ACS Nano* **2019**, *13*, 11891–11900.

[7] Guo, H. C.; Jia, K.; Han, S. J.; Zhao, H.; Qiu, B.; Xia, Y. G.; Liu, Z. P. Ultrafast heterogeneous nucleation enables a hierarchical surface configuration of lithium-rich layered oxide cathode material for enhanced electrochemical performances. *Adv. Mater. Interfaces* **2018**, *5*, 1701465.

[8] Tai, Z. G.; Zhu, W.; Shi, M.; Xin, Y. F.; Guo, S. W.; Wu, Y. F.; Chen, Y. Z.; Liu, Y. N. Improving electrochemical performances of lithium-rich oxide by cooperatively doping Cr and coating Li_3PO_4 as cathode material for lithium-ion batteries. *J. Colloid Interface Sci.* **2020**, *576*, 468–475.

[9] Yu, X. Q.; Lyu, Y.; Gu, L.; Wu, H. M.; Bak, S. M.; Zhou, Y. N.; Amine, K.; Ehrlich, S. N.; Li, H.; Nam, K. W. et al. Understanding the rate capability of high-energy-density Li-rich layered $Li_{1.2}Ni_{0.15}Co_{0.1}Mn_{0.55}O_2$ cathode materials. *Adv. Energy Mater.* **2014**, *4*, 1300950.

[10] Yang, S. Q.; Wang, P. B.; Wei, H. X.; Tang, L. B.; Zhang, X. H.; He, Z. J.; Li, Y. J.; Tong, H.; Zheng, J. C. $Li_4V_2Mn(PO_4)_4$-stablized $Li[Li_{0.2}Mn_{0.54}Ni_{0.13}Co_{0.13}]O_2$ cathode materials for lithium ion batteries. *Nano Energy* **2019**, *63*, 103889.

[11] Song, C. K.; Feng, W. J.; Shi, Z. J.; Huang, Z. Y. Coating TiO_2 on lithium-rich $Li_{1.2}Mn_{0.54}Ni_{0.13}Co_{0.13}O_2$ material to improve its electrochemical performance. *Ionics* **2021**, *27*, 457–468.

[12] Dong, S. D.; Zhou, Y.; Hai, C. X.; Zeng, J. B.; Sun, Y. X.; Ma, Y. F.; Shen, Y.; Li, X.; Ren, X. F.; Sun, C. et al. Enhanced cathode performance: Mixed Al_2O_3 and $LiAlO_2$ coating of $Li_{1.2}Ni_{0.13}Co_{0.13}Mn_{0.54}O_2$. *ACS Appl. Mater. Interfaces* **2020**, *12*, 38153–38162.

[13] Wang, M.; Chen, L.; Liu, M.; Chen, Y. B.; Gu, Y. J. Enhanced electrochemical performance of La-doped Li-rich layered cathode material. *J. Alloys Compd.* **2020**, *848*, 156620.

[14] Chen, M.; Chen, D. R.; Liao, Y. H.; Zhong, X. X.; Li, W. S.; Zhang, Y. G. Layered lithium-rich oxide nanoparticles doped with spinel phase: Acidic sucrose-assistant synthesis and excellent performance as cathode of lithium ion battery. *ACS Appl. Mater. Interfaces* **2016**, *8*, 4575–4584.

[15] El-Shinawi, H.; Greaves, C.; Janek, J. Sol–gel synthesis and room-temperature properties of α-$LiZr_2(PO_4)_3$. *RSC Adv.* **2015**, *5*, 17054–17059.

[16] Huang, L.; Liu, L.; Wu, H.; Wang, Y. J.; Liu, H.; Zhang, Y. Optimization of synthesis parameters for uniform sphere-like $Li_{1.2}Mn_{0.54}Ni_{0.13}Co_{0.13}O_2$ as high performance cathode material for lithium ion batteries. *J. Alloys Compd.* **2019**, *775*, 921–930.

[17] Yuan, X. L.; Xu, Q. J.; Liu, X. N.; Liu, H. M.; Min, Y. L.; Xia, Y. Y. Layered cathode material with improved cycle performance and capacity by surface anchoring of TiO_2 nanoparticles for Li-ion batteries. *Electrochim. Acta* **2016**, *213*, 648–654.

[18] Lee, H. J.; Lim, S. B.; Kim, J. Y.; Jeong, M.; Park, Y. J.; Yoon, W. S. Characterization and control of irreversible reaction in Li-rich cathode during the initial charge process. *ACS Appl. Mater. Interfaces* **2018**, *10*, 10804–10818.

[19] Liu, Y. C.; Chen, Y. F.; Wang, J.; Wang, W.; Ding, Z. Y.; Li, L. Y.; Zhang, Y.; Deng, Y. D.; Wu, J. W.; Chen, Y. N. Hierarchical yolk–shell structured Li-rich cathode boosting cycling and voltage stabled LIBs. *Nano Res.* **2022**, *15*, 3178–3186.

[20] Xiang, Y. H.; Sun, Z.; Li, J.; Wu, X. W.; Liu, Z. X.; Xiong, L. Z.; He, Z. Q.; Long, B.; Yang, C.; Yin, Z. L. Improved electrochemical performance of $Li_{1.2}Ni_{0.2}Mn_{0.6}O_2$ cathode material for lithium ion batteries synthesized by the polyvinyl alcohol assisted sol–gel method. *Ceram. Int.* **2017**, *43*, 2320–2324.

[21] Shi, J. L.; Qi, R.; Zhang, X. D.; Wang, P. F.; Fu, W. G.; Yin, Y. X.; Xu, J.; Wan, L. J.; Guo, Y. G. High-thermal-and air-stability cathode material with concentration-gradient buffer for Li-ion batteries. *ACS Appl. Mater. Interfaces* **2017**, *9*, 42829–42835.

[22] Wu, B.; Yang, X. K.; Jiang, X.; Zhang, Y.; Shu, H. B.; Gao, P.; Liu, L.; Wang, X. Y. Synchronous tailoring surface structure and chemical composition of Li-rich-layered oxide for high-energy lithium-ion batteries. *Adv. Funct. Mater.* **2018**, *28*, 1803392.

[23] Liu, Q.; Xie, T.; Xie, Q. S.; He, W.; Zhang, Y. G.; Zheng, H. F.; Lu, X. J.; Wei, W. S.; Sa, B.; Wang, L. S. et al. Multiscale deficiency integration by Na-rich engineering for high-stability Li-rich layered oxide cathodes. *ACS Appl. Mater. Interfaces* **2021**, *13*, 8239–8248.

[24] Zhang, J. F.; Zhang, J. Y.; Ou, X.; Wang, C. H.; Peng, C. L.; Zhang, B. Enhancing high-voltage performance of Ni-rich cathode by surface modification of self-assembled NASICON fast ionic conductor $LiZr_2(PO_4)_3$. *ACS Appl. Mater. Interfaces* **2019**, *11*, 15507–15516.

[25] Pang, S. L.; Zhu, M.; Xu, K. J.; Shen, X. Q.; Wen, H. R.; Su, Y. J.; Yang, G. M.; Wu, X.; Li, S. W.; Wang, W. Z. et al. Enhanced electrochemical performance of $Li_{1.2}Mn_{0.54}Ni_{0.13}Co_{0.13}O_2$ via L-ascorbic acid-based treatment as cathode material for Li-ion batteries. *J. Electrochem. Soc.* **2018**, *165*, A1897–A1902.

[26] Jiao, L. F.; Zhang, M.; Yuan, H. T.; Zhao, M.; Guo, J.; Wang, W.; Zhou, X. D.; Wang, Y. M. Effect of Cr doping on the structural, electrochemical properties of $Li[Li_{0.2}Ni_{0.2-x/2}Mn_{0.6-x/2}Cr_x]O_2$ (x = 0, 0.02, 0.04, 0.06, 0.08) as cathode materials for lithium secondary batteries. *J. Power Sources* **2007**, *167*, 178–184.

[27] Li, J.; Klöpsch, R.; Stan, M. C.; Nowak, S.; Kunze, M.; Winter, M.; Passerini, S. Synthesis and electrochemical performance of the high voltage cathode material $Li[Li_{0.2}Mn_{0.56}Ni_{0.16}Co_{0.08}]O_2$ with improved rate capability. *J. Power Sources* **2011**, *196*, 4821–4825.

[28] Li, L. J.; Xu, M.; Chen, Z. Y.; Zhou, X.; Zhang, Q. B.; Zhu, H. L.; Wu, C.; Zhang, K. L. High-performance lithium-rich layered oxide materials: Effects of chelating agents on microstructure and electrochemical properties. *Electrochim. Acta* **2015**, *174*, 446–455.

[29] Moses, A. W.; Flores, H. G. G.; Kim, J. G.; Langell, M. A. Surface properties of $LiCoO_2$, $LiNiO_2$ and $LiNi_{1-x}Co_xO_2$. *Appl. Surf. Sci.* **2007**, *253*, 4782–4791.

[30] Li, J. G.; Wang, L.; Zhang, Q.; He, X. M. Synthesis and characterization of $LiNi_{0.6}Mn_{0.4-x}Co_xO_2$ as cathode materials for Li-ion batteries. *J. Power Sources* **2009**, *189*, 28–33.

[31] Jiang, X. D.; Wei, Y.; Yu, X. H.; Dong, P.; Zhang, Y. J.; Zhang, Y. N.; Liu, J. X. $CeVO_4$-coated $LiNi_{0.6}Co_{0.2}Mn_{0.2}O_2$ as positive material: Towards the excellent electrochemical performance at normal and high temperature. *J. Mater. Sci. :Mater. Electron.* **2018**, *29*, 15869–15877.

[32] Hao, Y. X.; Yang, F. N.; Luo, D. D.; Tian, J. H.; Shan, Z. Q. Improved electrochemical performances of yttrium oxyfluoride-coated $Li[Li_{0.2}Mn_{0.54}Ni_{0.13}Co_{0.13}O_2]$ for lithium ion batteries. *J. Energy Chem.* **2018**, *27*, 1239–1246.

[33] Lai, X. W.; Hu, G. R.; Peng, Z. D.; Tong, H.; Lu, Y.; Wang, Y. Z.; Qi, X. Y.; Xue, Z. C.; Huang, Y.; Du, K. et al. Surface structure decoration of high capacity $Li_{1.2}Mn_{0.54}Ni_{0.13}Co_{0.13}O_2$ cathode by mixed conductive coating of $Li_{1.4}Al_{0.4}Ti_{1.6}(PO_4)_3$ and polyaniline for lithium-ion batteries. *J. Power Sources* **2019**, *431*, 144–152.

[34] Ji, X. Q.; Xu, Y. X.; Feng, H. L.; Wang, P. F.; Zhou, Y. C.; Song, J. C.; Xia, Q.; Tan, Q. Q. Surface $LiMn_{1.4}Ni_{0.5}Mo_{0.1}O_4$ coating and bulk Mo doping of Li-rich Mn-based $Li_{1.2}Mn_{0.54}Ni_{0.13}Co_{0.13}O_2$ cathode with enhanced electrochemical performance for lithium-ion batteries. *ACS Appl. Mater. Interfaces* **2021**, *13*, 47659–47670.

[35] Shi, J. L.; Xiao, D. D.; Zhang, X. D.; Yin, Y. X.; Guo, Y. G.; Gu, L.; Wan, L. J. Improving the structural stability of Li-rich cathode materials via reservation of cations in the Li-slab for Li-ion batteries. *Nano Res.* **2017**, *10*, 4201–4209.

[36] Chen, M.; Xiang, X. D.; Chen, D. R.; Liao, Y. H.; Huang, Q. M.; Li, W. S. Polyethylene glycol-assisted synthesis of hierarchically porous layered lithium-rich oxide as cathode of lithium ion battery. *J. Power Sources* **2015**, *279*, 197–204.

[37] Yabuuchi, N.; Yoshii, K.; Myung, S. T.; Nakai, I.; Komaba, S. Detailed studies of a high-capacity electrode material for rechargeable batteries, Li_2MnO_3-$LiCo_{1/3}Ni_{1/3}Mn_{1/3}O_2$. *J. Am. Chem. Soc.* **2011**, *133*, 4404–4419.

[38] Bao, Y. B.; Wang, J.; Qian, Y. X.; Deng, Y. F.; Yang, X. F.; Chen, G. H. An appropriate amount of new spinel phase induced by control synthesis for the improvement of electrochemical performance of Li-rich layered oxide cathode material. *Electrochim. Acta* **2020**, *330*, 135240.

[39] Li, G. H.; Ren, Z. M.; Li, A. L.; Yu, R. Z.; Quan, W.; Wang, C. H.; Lin, T.; Yi, D.; Liu, Y.; Zhang, Q. H. et al. Highly stable surface and structural origin for lithium-rich layered oxide cathode materials. *Nano Energy* **2022**, *98*, 107169.

[40] Chen, B. Z.; Zhao, B. C.; Zhou, J. F.; Fang, Z. T.; Huang, Y. N.; Zhu, X. B.; Sun, Y. P. Surface modification with oxygen vacancy in Li-rich layered oxide $Li_{1.2}Mn_{0.54}Ni_{0.13}Co_{0.13}O_2$ for lithium-ion batteries. *J. Mater. Sci. Technol.* **2019**, *35*, 994–1002.

[41] Yi, T. F.; Li, Y. M.; Yang, S. Y.; Zhu, Y. R.; Xie, Y. Improved cycling stability and fast charge–discharge performance of cobalt-free lithium-rich oxides by magnesium-doping. *ACS Appl. Mater. Interfaces* **2016**, *8*, 32349–32359.

[42] Yi, T. F.; Han, X.; Yang, S. Y.; Zhu, Y. R. Enhanced electrochemical performance of Li-rich low-Co $Li_{1.2}Mn_{0.56}Ni_{0.16}Co_{0.08-x}Al_xO_2$ ($0 \le x \le 0.08$) as cathode materials. *Sci. China Mater.* **2016**, *59*, 618–628.

[43] Yi, T. F.; Chen, B.; Zhu, Y. R.; Li, X. Y.; Zhu, R. S. Enhanced rate performance of molybdenum-doped spinel $LiNi_{0.5}Mn_{1.5}O_4$ cathode materials for lithium ion battery. *J. Power Sources* **2014**, *247*, 778–785.

[44] Zhou, Z. W.; Luo, Z. Y.; He, Z. J.; Zheng, J. C.; Li, Y. J.; Yan, C.; Mao, J. Suppress voltage decay of lithium-rich materials by coating layers with different crystalline states. *J. Energy Chem.* **2021**, *60*, 591–598.